crystals

MDPI

Article

A Systematic Study of Compositionally Dependent Dielectric Tensors of $\mathrm{SnS}_x\mathrm{Se}_{1-x}$ Alloys by Spectroscopic Ellipsometry

Xuan Au Nguyen [1,†], Thi Minh Hai Nguyen [2,†], Tae Jung Kim [1,3,*], Long Van Le [1,4], Tung Hoang Nguyen [1,4], Bogyu Kim [1], Kyujin Kim [1], Wonjun Lee [1], Sunglae Cho [2,*] and Young Dong Kim [1,*]

[1] Department of Physics, Kyung Hee University, Seoul 02447, Korea; xuanau@khu.ac.kr (X.A.N.); lelong@khu.ac.kr (L.V.L.); tungnh@khu.ac.kr (T.H.N.); kbk4844@khu.ac.kr (B.K.); kujinning@khu.ac.kr (K.K.); wonjunid@khu.ac.kr (W.L.)

[2] Department of Physics and Energy Harvest-Storage Research Center, University of Ulsan, Ulsan 44610, Korea; minhhai0204@gmail.com

[3] Center for Converging Humanities, Kyung Hee University, Seoul 02447, Korea

[4] Institute of Materials Science, Vietnam Academy of Science and Technology, Hanoi 100000, Vietnam

[*] Correspondence: tjkim@khu.ac.kr (T.J.K.); slcho@ulsan.ac.kr (S.C.); ydkim@khu.ac.kr (Y.D.K.)

[†] These authors contributed equally to this work.

Abstract: We report the dielectric tensors on the cleavage plane of biaxial $\mathrm{SnS}_x\mathrm{Se}_{1-x}$ alloys in the spectral energy region from 0.74 to 6.42 eV obtained by spectroscopic ellipsometry. Single-crystal $\mathrm{SnS}_x\mathrm{Se}_{1-x}$ alloys were grown by the temperature-gradient method. Strongly anisotropic optical responses are observed along the different principal axes. An approximate solution yields the anisotropic dielectric functions along the zigzag (*a*-axis) and armchair (*b*-axis) directions. The critical point (CP) energies of $\mathrm{SnS}_x\mathrm{Se}_{1-x}$ alloys are obtained by analyzing numerically calculated second derivatives, and their physical origins are identified by energy band structure. Blue shifts of the CPs are observed with increasing S composition. The fundamental bandgap for Se = 0.8 and 1 in the armchair axis arises from band-to-band transitions at the M_0 minimum point instead of the M_1 saddle point as in SnS. These optical data will be useful for designing optoelectronic devices based on $\mathrm{SnS}_x\mathrm{Se}_{1-x}$ alloys.

Keywords: SnSSe alloy; anisotropic dielectric tensor; ellipsometry

Citation: Nguyen, X.A.; Nguyen, T.M.H.; Kim, T.J.; Le, L.V.; Nguyen, T.H.; Kim, B.; Kim, K.; Lee, W.; Cho, S.; Kim, Y.D. A Systematic Study of Compositionally Dependent Dielectric Tensors of $\mathrm{SnS}_x\mathrm{Se}_{1-x}$ Alloys by Spectroscopic Ellipsometry. *Crystals* **2021**, *11*, 548. https://doi.org/10.3390/cryst11050548

Academic Editor: Pavel Lukáč

Received: 11 April 2021
Accepted: 11 May 2021
Published: 14 May 2021

1. Introduction

Recently, Sn-X (X = S, Se) and their alloys have received much attention not only due to their potential in applications for ion batteries [1], sensors [2], thermoelectric devices [3–13], and photovoltaics [14–19] but also for their chemical stability and lower toxicity relative to other compounds that use heavy metals such as lead or cadmium. $\mathrm{SnS}_x\mathrm{Se}_{1-x}$ alloys $0 \leq x \leq 1$ crystallize in an orthorhombic structure belonging to the space group Pnma, which consists of valence bonds between each Sn atom and three adjacent X atoms to form a puckered honeycomb network, resulting in strong (*ab*-axis) in-plane anisotropy. In the *c*-direction, the Sn-X layers are separated by weak van der Waals bonding. The crystal structure and Brillouin zone of SnSe are given in Figure 1.

Complex dielectric function $\varepsilon = \varepsilon_1 + i\varepsilon_2$ or refractive index $\tilde{N} = n + ik$ values provide useful insight into electronic structure and for characterizing device performance [20–22]. Many studies have reported the optical properties of Sn-X by absorption and reflection [23,24], photoluminescence [25–27], photoreflectance [28], and ultraviolet-visible-near infrared spectroscopy [13]. Among optical measurements, we used spectroscopic ellipsometry (SE) because it directly determines the dielectric function and refractive index of a material [29–31] without using the Kramers–Kronig relations. A few studies of the dielectric functions of SnS and SnSe have been reported [32–35], but there has been no systematic investigation so far of the dependence of the dielectric functions on S and Se compositions.

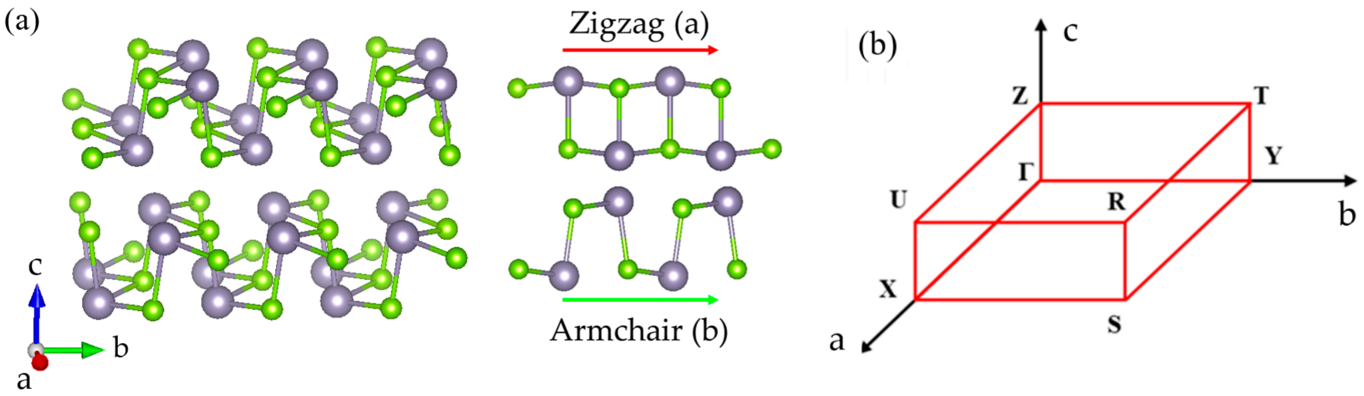

Figure 1. (**a**) Distorted-rocksalt orthorhombic (Pnma) crystal structure of SnSe. The Sn atoms are purple, while the Se atoms are green. (**b**) Brillouin zone of the SnSe structure.

In this work, we present the composition-dependent dielectric tensors of SnS_xSe_{1-x} (x = 0, 0.2, 0.42, 0.52, 0.6, 0.82, and 1) on the cleavage (001) plane from 0.74 to 6.42 eV at room temperature (RT). These tensor components correspond to the zigzag (*a*-axis) and armchair (*b*-axis) directions, specifically. A multilayer-model calculation was performed to remove the effect of surface roughness and/or surface contamination. Blue shifts of the critical points (CPs) are observed with increasing S composition. From these data we determine the CP energies by fitting numerically calculated second derivatives to standard analytic expressions. Energy band calculations were done using the modified Becke–Johnson (mBJ) method for bandgap correction to determine the band-to-band transitions of each CP. We also find that the fundamental band gap of SnSe arises from the M_0 minimum, while it is at the M_1 saddle point in SnS along the armchair direction.

2. Experimental Methods and ab Initio Calculations

Single-crystal SnS_xSe_{1-x} (x = 0, 0.2, 0.42, 0.52, 0.6, 0.82, and 1) were grown by the temperature-gradient method, where powders of tin (99.8%), sulfur (99%), and selenium (99%) were weighted at an appropriate molecular ratio [36,37]. The composition of elements was confirmed by Energy-Dispersive X-ray spectroscopy and structure of the samples were determined by X-ray diffraction (XRD). The XRD measurement and analysis are explained in detailed in Ref. [37]. Before SE measurements, the samples were peeled on the cleavage surface (mechanical exfoliation) to eliminate contamination, surface oxides, and overlayer artifacts. The surface roughness of the cleavage (001) was determined using Atomic force microscopy (AFM)(XE-100 Park System) to provide the thickness values of the rough surface for multilayer calculations.

Pseudodielectric functions were measured at room temperature using a M2000-DI ellipsometer (J. A. Woollam Co., Inc., Lincoln, NE, USA), which has a spectral range of 0.74 to 6.42 eV. To determine the fundamental *a*- and *b*-axes on the cleavage plane, azimuthal pseudodielectric function data were obtained as shown in Figure 2a for $SnS_{0.52}Se_{0.48}$, as an example. The zero corresponds to the armchair direction (*b*-axis). The angle of incidence (AOI) for this measurement was 70°, although this is not critical for this procedure. The strongly anisotropic behavior of the pseudodielectric function is clearly observed. The full rotation of azimuthal angle was performed to determine the orientation of *a*- and *b*-axes precisely, as shown in Figure 2b, confirming the sample orientation given by the XRD in Ref. [37].

It is well known that the dominant contribution for ellipsometric measurement is the projection of the dielectric tensor onto the line of intersection between the sample surface and plane of incidence (POI) Refs. [38,39]. Therefore, even though the measurement was carried out on the SnS_xSe_{1-x} along the zigzag (*a*-axis) and armchair (*b*-axis) directions precisely, as shown in Figure 3a,b, respectively, the measured pseudodielectric functions vary with the AOI, showing clear existence of strong optical anisotropy.

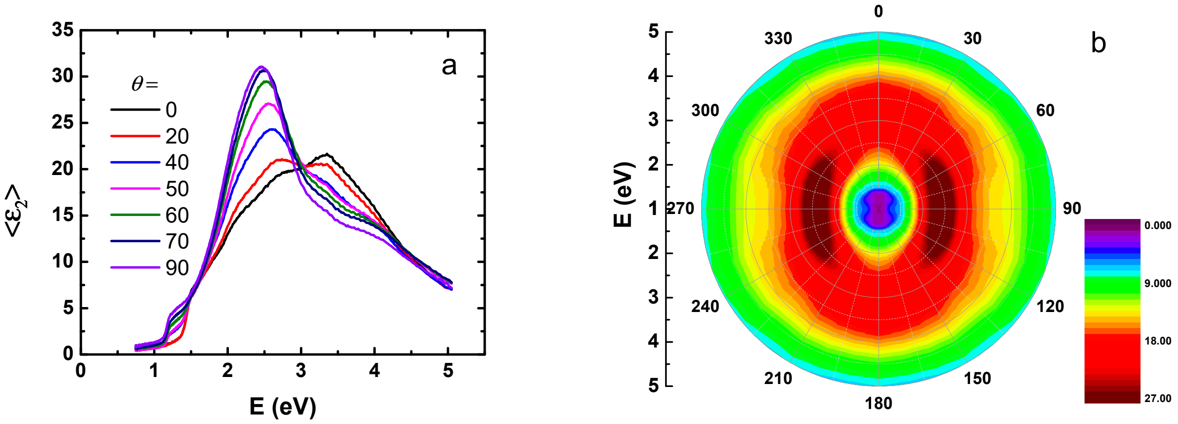

Figure 2. (**a**) Azimuthal angle dependence of the dielectric function from the armchair- to zigzag-directions at AOI = 70°. (**b**) Mapping of the full azimuthal angles of the dielectric function of single-crystal $SnS_{0.52}Se_{0.48}$.

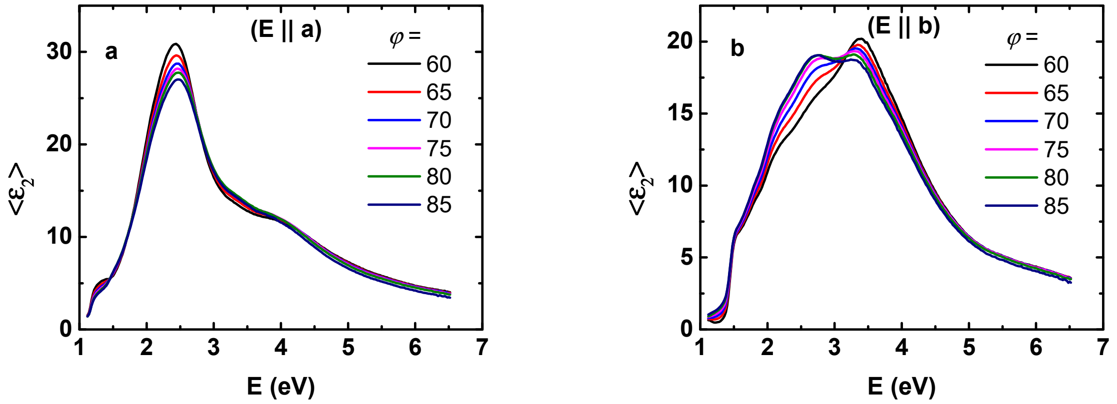

Figure 3. Imaginary parts of the pseudodielectric functions of $SnS_{0.52}Se_{0.48}$ with several values of AOI from 60° to 85° along (**a**) zigzag and (**b**) armchair directions.

The intrinsic dielectric tensor of all three principal axes of biaxial materials can be accurately obtained by generalized ellipsometry [40–42]. However, it requires a complicated measurement process in which data at several AOIs and azimuthal angles are necessary for the analysis. The data analysis process also requires plenty of efforts. Besides this method, the approximation method introduced by Aspnes [38,39] can also be used to determine the dielectric function of anisotropic materials. This method has been used to study optical properties of both bulk and thin-film samples [37,38,42] due to it is easier in data processing but still preserves important insight of the measurements. It applies well to the case where only two axes are measured, for example, thin-film and layered samples [38,43] when measuring the *c*-axis becomes too difficult. Therefore, we adopted the latter method for our data analysis.

Briefly, this assumes that the dielectric tensor components ε_a, ε_b, and ε_c can be obtained by applying small corrections to an isotropic mean value $\bar{\varepsilon}$, i.e.,

$$\varepsilon_i = \bar{\varepsilon} + \Delta\varepsilon_i, \quad i = a, b, c. \tag{1}$$

The correction $\Delta\varepsilon_i$ can be treated in first order when solving the simultaneous linear equations

$$\frac{\bar{\varepsilon} - \sin^2\varphi}{\bar{\varepsilon} - 1}\Delta\varepsilon_i - \frac{\bar{\varepsilon}\cos^2\varphi - \sin^2\varphi}{\bar{\varepsilon} - 1}\Delta\varepsilon_j - \frac{\sin^2\varphi}{\bar{\varepsilon} - 1}\Delta\varepsilon_k = (\varepsilon_{ik} - \varepsilon) sin^2\varphi \tag{2}$$

where ik = (ac, bc, ca) or another selection of pairs of principal axes defining three planes of incidence, and φ is the angle of incidence. The i, j, k indices are construed as following order: $i = (a, b, c)$, $j = (b, c, a)$, $k = (c, a, b)$. Therefore, Equation (2) represents the three equations along the three planes of incidence. For example, the dielectric function ε_{ik} is obtained from the plane of incidence ik where the light propagates along the i direction. Therefore, ε_{ac} and ε_{ca} are dielectric functions of two different directions in the same plane of incidence. The mean value $\bar{\varepsilon}$ is calculated from the data $\varepsilon_{ik}(ac, bc, ca)$ in the Bruggeman effective-medium approximation [44] using equal admixtures of the three components:

$$f_{ac}\frac{\varepsilon_{ac}-\bar{\varepsilon}}{\varepsilon_{ac}+2\bar{\varepsilon}}+f_{bc}\frac{\varepsilon_{bc}-\bar{\varepsilon}}{\varepsilon_{bc}+2\bar{\varepsilon}}+f_{ca}\frac{\varepsilon_{ca}-\bar{\varepsilon}}{\varepsilon_{ca}+2\bar{\varepsilon}}=0 \tag{3}$$

Because the pseudodielectric tensors of biaxial materials approach their intrinsic values as the AOI approaches 90° [39], it is best to perform SE measurements at large AOIs. However, even at 80° and 85°, light scattering on the sample surface generates substantial noise in the data. Therefore, we selected 75° as the AOI. This is widely used to determine anisotropic dielectric functions [32–35,38,39]. Figure 4 show the measured pseudodielectric function at AOI = 75° along with spectra from the approximation solution, showing that the measurements at 75° represents the intrinsic principal component of dielectric tensor reasonably well. The intrinsic components of the dielectric tensor were extracted via the three phase (ambient/surface roughness/sample) model.

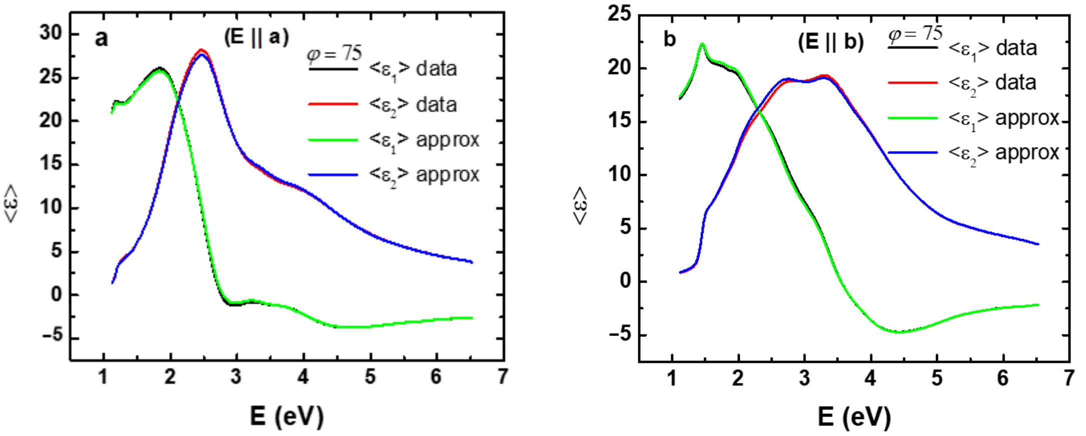

Figure 4. The pseudodielectric function of $SnS_{0.52}Se_{0.48}$ along zigzag direction (**a**) and armchair direction (**b**) measured at AOI = 75° (black and red) and the resulting data (green and blue) after approximation method was applied.

To identify the physical origins of the CP structures, first-principles density-functional-theory (DFT) calculations were performed within the framework of the projector-wave formalism [45], as implemented in the Vienna ab initio simulation package (VASP). A detailed explanation is given in Ref. [35]. The generalized gradient approximation (GGA) with Perdew, Burke, and Ernzerhof (PBE) parameterization was used to describe the exchange-correlation functional [46,47]. Since the GGA generally underestimates bandgap values, the mBJ exchange potential in combination with L(S)DA-correlation [48,49] was used to achieve actual band gaps. The plane-wave cutoff for the kinetic energy was 350 eV. Brillouin integration was done with a 8 × 8 × 4 centered k-points grid. The structural parameters of SnS and SnSe were fixed at the experimentally determined values from Ref. [50], where a = 3.98 Å, b = 4.33 Å, and c = 11.18 Å for SnS, while a = 4.19 Å, b=4.46 Å, and c = 11.57 Å for SnSe.

3. Results and Discussion

Figure 5a,b show the imaginary parts of the resulting dielectric functions along the a- and b-axes of SnSe and SnS, respectively obtained by the approximation solution. Due to anisotropic nature of these materials, the significant differences between the zigzag and armchair directions are clearly seen in the black and red curves, respectively. The blue shift of the CPs observed when Se is replaced by S is obvious. This is also observed in other semiconductors, for example ZnS and ZnSe [51–53] and GeS and GeSe [39,54,55]. Within the same material, however, the CPs along the different principal axes have similar energy positions, which will be identified below from band structure calculations.

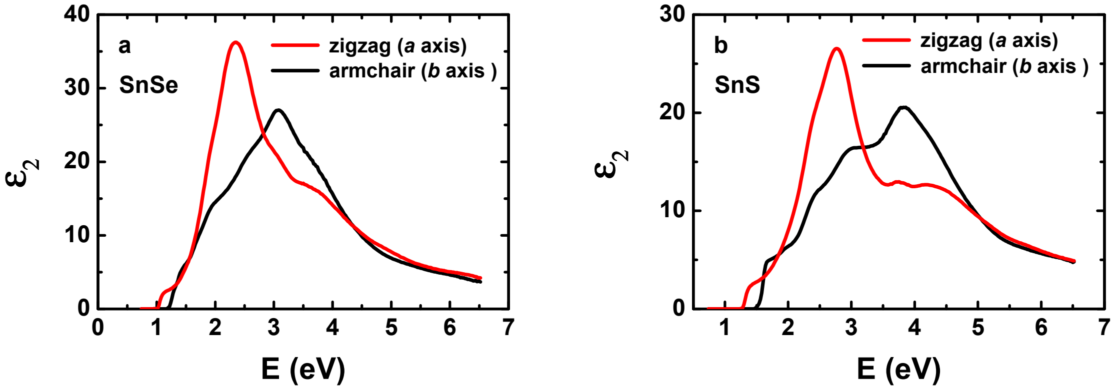

Figure 5. Comparison of the imaginary parts of the dielectric functions along the zigzag and armchair directions of SnSe (**a**) and SnS (**b**).

Figure 6a,b show the real and imaginary parts of the extracted dielectric functions, respectively, of SnS_xSe_{1-x} along the *a*-axis. For clarity, the spectra are offset by increments of 10 relative to that of $x = 1$. The decrease of the CP energies is clearly observed from SnS ($x = 1$) to SnSe ($x = 0$) as indicated in Figure 6b. Similarly, Figure 7a,b show the real and imaginary parts of the extracted dielectric functions along the *b*-axis, respectively, showing the same decrease of the CP peak positions with decreasing S component. We note that the cleavage surface of SnS_xSe_{1-x} is considered to be stable and to oxidize insignificantly in air for a few hours at room temperature [32]. However, we were more cautions, refreshing the sample surface by mechanical exfoliation before each SE measurement. Using this precaution, we find that our resulting spectra are in good agreement with previously reported data in Refs. [32,33], confirming that current data represent the intrinsic dielectric response of the SnS_xSe_{1-x} alloys.

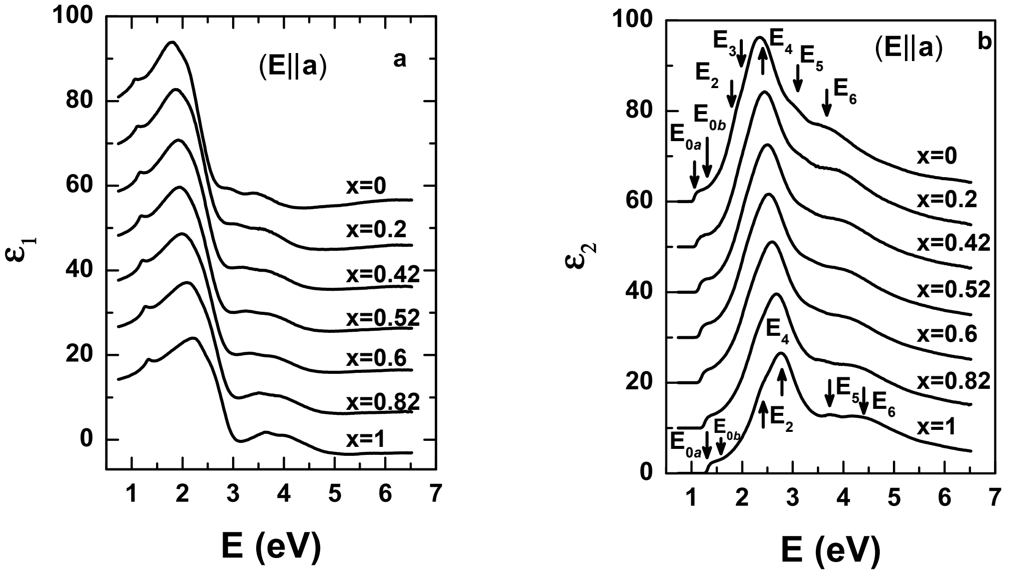

Figure 6. Real (**a**) and imaginary (**b**) parts of the dielectric functions of SnS_xSe_{1-x} along the zigzag direction. The spectra are shifted by increments of 10 from that at $x = 1$.

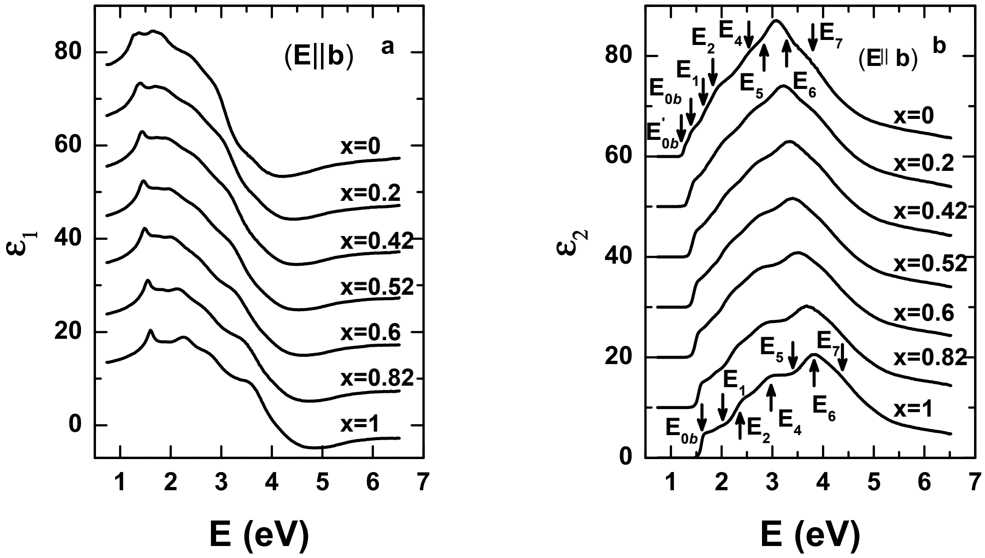

Figure 7. Real (**a**) and imaginary (**b**) parts of the dielectric functions of SnS_xSe_{1-x} along the armchair direction. The spectra are shifted by increments of 10 from that at $x = 1$.

The CP energies were determined by fitting the SE data to the standard line-shape expressions [56] where the dielectric function spectra are differentiated. Noise removal of the spectra was performed using algorithms of extended Gaussian filtering [57] with removal of endpoint discontinuity artifacts [58]. The CP expressions are:

$$\frac{d^2 < \varepsilon >}{dE^2} = \begin{cases} A(n-1)e^{i\phi}(E - E_g + i\Gamma)^{n-2}, n \neq 0 \\ Ae^{i\phi}(E - E_g + i\Gamma)^{-2}, n = 0 \end{cases} \quad (4)$$

where A is the amplitude, E_g is the threshold energy, Γ is the broadening parameter, and ϕ is the phase. The exponent n has values of -1, $-1/2$, 0, and $1/2$ for excitonic, one-, two-, and three-dimensional line-shapes, respectively. Real and imaginary parts are fit simultaneously.

Figures 8 and 9 show the second derivatives of the two principal axes and their best fits of SnS_xSe_{1-x} with x = 0, 0.52, and 1. Open circles are calculated spectra $d^2\varepsilon_1/dE^2$, while the solid and the dashed lines are the best fits of the CP expressions for $d^2\varepsilon_1/dE^2$ and $d^2\varepsilon_2/dE^2$, respectively. The data for $d^2\varepsilon_2/dE^2$ are not shown for clarity. We note that the excitonic line-shape ($n = -1$) yields the best fit for all the CPs. In Figure 8, a careful inspection of the a-axis spectra reveals the existence of the E_3 CP in SnSe, while it is absent in SnS. We note that the E_3 CP in SnS can be detected only at low-temperature Ref. [34]. In Figure 9 of the b-axis spectra, another interesting observation is the splitting of the direct fundamental bandgap of E_{0b} in SnS into E_{0b} and E'_{0b} in SnSe. The physical origin of new E'_{0b} CP will be considered below.

Figures 10 and 11 show the results of energy band structure calculations obtained using the mBJ method for bandgap correction of SnSe and SnS, respectively, in which the band-to-band transitions corresponding to the CPs in above discussions are denoted by arrows. As shown in Figures 10 and 11, the top of valence band (VB) is located along the $\Gamma - Y$ line (parallel to b-axis in real space), while the bottom of conduction band (CB) is at the $\Gamma - X$ line (a-axis direction). Therefore, the direct optical transition is not allowed in this situation. In the band structure the fundamental direct band gap E_{0a} is expected to occur between the first VB and the first CB in the $\Gamma - X$ line for both SnS and SnSe. As listed in Tables 1 and 2, the measured values for SnSe and SnS are about 1.06 and 1.33 eV, respectively, while the calculated results are 0.97 and 1.33 eV. The agreement between data and theoretical predictions is therefore excellent. It is also interesting to note that in the $\Gamma - Y$ line, the smallest direct band gap E'_{0b} is predicted to be the M_0 minimum CP in SnSe, while the smallest direct band gap E_{0b} is at M_1 saddle point CP in SnS. This is a result of the different chemistries of Se and S. It should be noted that the current approach deals only with energy differences between valence and conduction bands [59–61]. To be physically more precise, the momentum operator between the bands needs to be considered to clarify whether the transitions are allowed and what polarizations are needed to detect them.

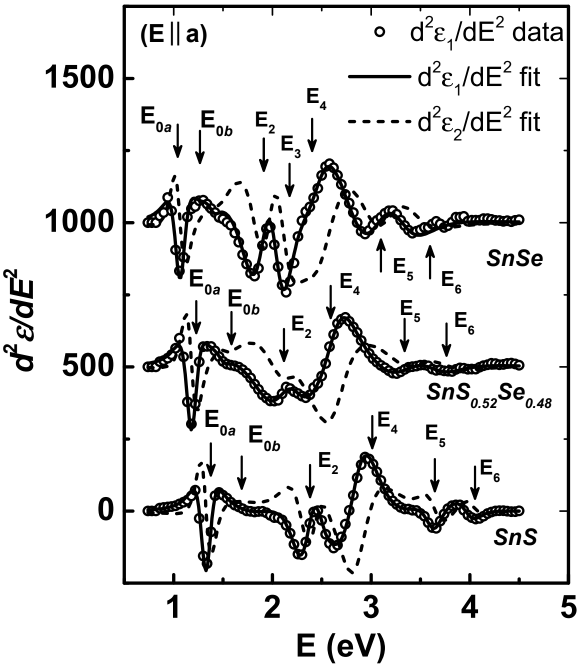

Figure 8. Best fits of the second derivatives of ε_1 (solid lines) and ε_2 (dashed lines) for the zigzag direction. The circles are the numerically calculated derivatives of the data. The number of points is reduced for clarity. The spectra are shifted by increments of 500 from that at $x = 1$.

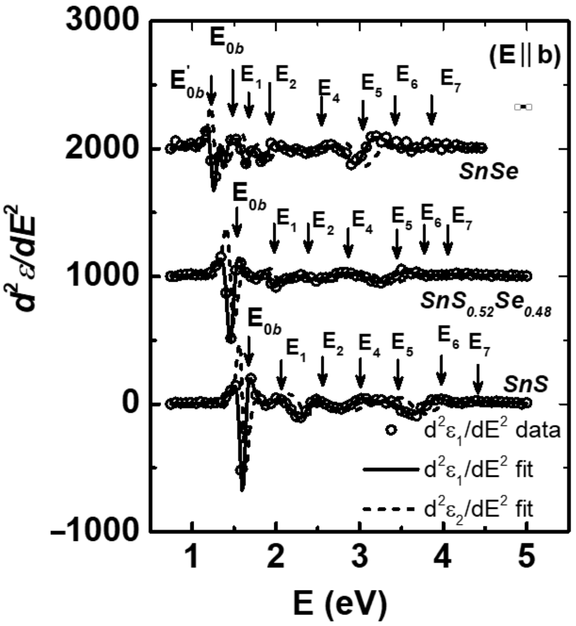

Figure 9. As Figure 8, for the armchair direction. The spectra are shifted by increments of 1000 from that at $x = 1$.

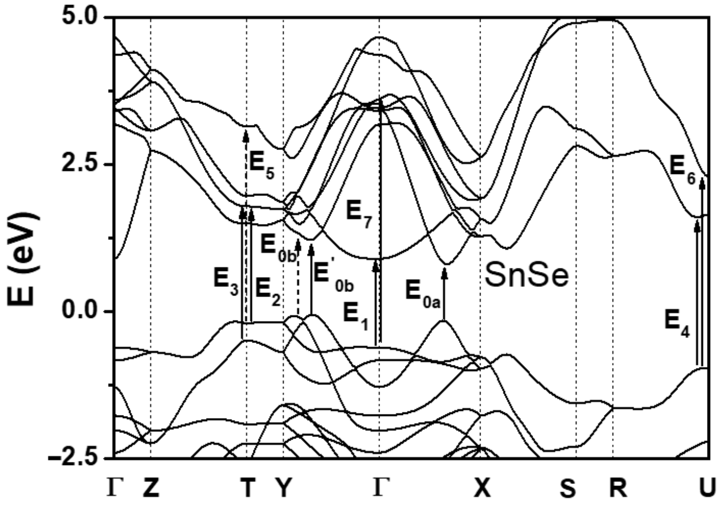

Figure 10. The calculated energy band structure of SnSe. Band-to-band transitions are shown by arrows. The dashed line is E_{0b}.

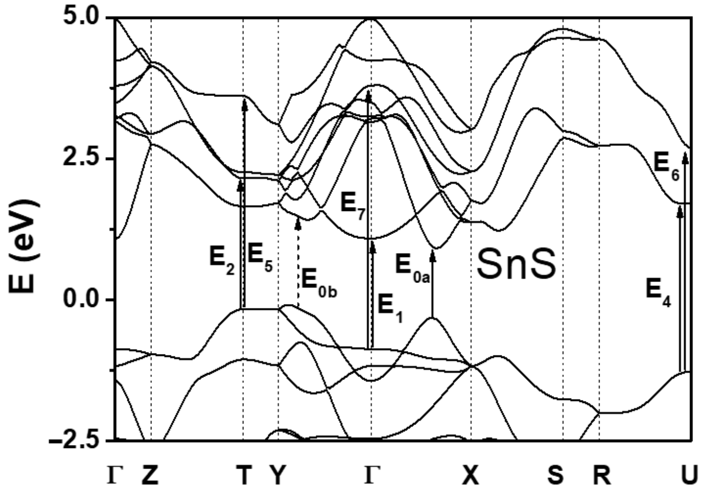

Figure 11. As Figure 10, but for SnS.

Table 1. Comparison of room temperature CP energies of SnSe obtained along the *a*- and *b*-axes with those predicted from the 0 K energy band structure shown in Figure 10.

CP	SnSe		
	Theory	***a*-Axis**	***b*-Axis**
E_{0a}	0.97 [a]—$\Gamma - X$	1.06 [a]	
E'_{0b}	1.20 [a]—$\Gamma - Y$		1.21 [a]
E_{0b}	1.37 [a]—$\Gamma - Y$	1.31 [a], 1.26 [d]	1.37 [a], 1.35 [d]
E_1	1.49 [a]—$\Gamma(0, 0, 0)$		1.65 [a], 1.64 [d]
E_2	1.90 [a]—$T(0, 0.5, 0.5)$	1.90 [a], 1.81 [d]	1.85 [a], 1.86 [d]
E_3	2.24 [a]—$T(0, 0.5, 0.5)$	2.23 [a], 2.14 [d]	
E_4	2.62 [a]—$U(0.5, 0, 0.5)$	2.33 [a], 2.31 [d]	2.56 [a], 2.43 [d]
E_5	3.29 [a]—$T(0, 0.5, 0.5)$		2.99 [a], 3.06 [d]
E_6	3.32 [a]—$U(0.5, 0, 0.5)$	3.02 [a], 2.91 [d]	3.25 [a]
E_7	4.20 [a]—$\Gamma(0, 0, 0)$	3.41 [a], 3.83 [d]	3.68 [a], 3.58 [d]

[a] This work—Exp RT, Theory 0 K. [d] Ref. [33]—Exp RT.

Table 2. As Table 1, for SnS.

CP	SnS		
	Theory	***a*-Axis**	***b*-Axis**
E_{0a}	1.33 ^{a}—$\Gamma - X$	1.33 ^{a}, 1.31 ^{b}	
E_{0b}	1.72 ^{a}—$\Gamma - Y$	1.65 ^{a}, 1.60 ^{b}, 1.59 ^{c}	1.60 ^{a}, 1.59 ^{b}
E_1	1.87 ^{a}—$\Gamma(0,0,0)$		1.90 ^{a}, 1.98 ^{b}, 1.91 ^{c}
E_2	2.40 ^{a}—$T(0,0.5,0.5)$	2.36 ^{a}, 2.34 ^{b}, 2.35 ^{c}	2.32 ^{a}, 2.28 ^{b}, 2.36 ^{c}
E_4	3.08 ^{a}—$U(0.5,0,0.5)$	2.83 ^{a}, 2.76 ^{b}, 2.80 ^{c}	2.92 ^{a}, 2.98 ^{b}, 2.82 ^{c}
E_5	3.80 ^{a}—$T(0,0.5,0.5)$		3.44 ^{a}, 3.29 ^{b}, 3.47 ^{c}
E_6	4.04 ^{a}—$U(0.5,0,0.5)$	3.64 ^{a}, 3.70 ^{b}, 3.68 ^{c}	3.88 ^{a}, 3.71 ^{b}, 3.70 ^{c}
E_7	4.55 ^{a}—$\Gamma(0,0,0)$	3.98 ^{a}, 4.06 ^{b}	4.24 ^{a}, 4.30 ^{b}, 4.41 ^{c}

[a] This work—Exp RT, Theory 0 K. [b] Ref. [33]—Exp RT. [c] Ref. [5]—Exp 295 K.

The full comparison of measured CP energies along the *a*- and *b*-axes with those predicted by the current band calculations are also shown in Tables 1 and 2 for SnSe and SnS, respectively. Considering that the band calculations assume 0 K while the measured CP energies are obtained at room temperature, the two results are reasonably well matched. Slightly different CP energies measured in *a*- and *b*-axes can be understood by the different slopes at symmetric points along the different directions in the Brillouin zone, which can lead to different intensities and line-shapes of the CPs. We also note that the overlap of adjacent CPs can cause uncertainties in the CP energy positions determined by experiment. The CP energies found in previous works are also included for comparison in Tables 1 and 2, and it is clear that our data are in good agreement with the results of these studies [5,22,23]. However, since ellipsometry determines the real and imaginary parts of dielectric functions without Kramers–Kronig relation, we believe that the current work should be more accurate than the results obtained from the reflectance measurement of Ref. [5]. Relative to the previous ellipsometric studies of Refs. [32,33], we observed more CP structures, and our data exhibit zero values of the imaginary part of the dielectric function below the fundamental band gap. These results indicate that our CP results are more accurate.

To allow CP energies to be determined for any composition, we fit the quadratic $E(x) = ax^2 + bx + c$ to the data as shown in Figures 12 and 13 for the zigzag and armchair directions, respectively. The dots are data, while the solid curves are best fits. It is interesting to note that the E_5 CP shows negative bowing, while other show the positive bowings characteristic of semiconductor alloys in general [62–64]. Irrespective of attractive or repulsive atomic interactions, if an interaction exists between energy states, the corresponding states repel each other. We understand that the negative bowing of the E_5 structure in Figure 13 might have resulted from the proximity of the E_6 CP, which may result in interaction larger in armchair direction. The values of *a*, *b*, and *c* are listed in Tables 3 and 4 for the zigzag and armchair directions, respectively.

Table 3. Fitted parameter values of quadratic equations for allowing composition dependences of the CP energies along the zigzag direction to be determined.

CP	*c*	*b*	*a*
E_{0a}	1.0591	0.2208	0.0443
E_{0b}	1.3135	0.2404	0.0943
E_2	1.9049	0.0641	0.3997
E_3	2.2326	0.3654	0
E_4	2.3257	0.3055	0.1987
E_5	3.0126	0.1776	0.4509
E_6	3.4121	0.2852	0.2863

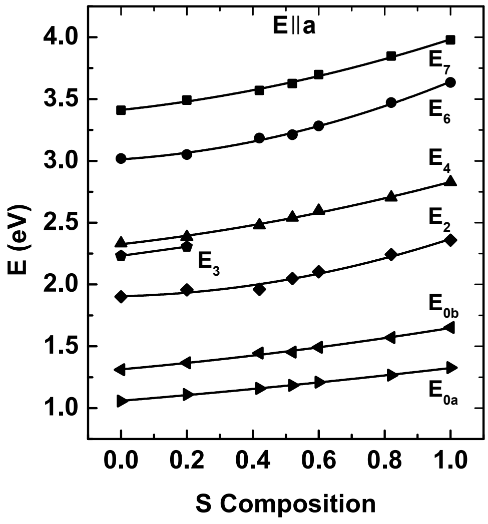

Figure 12. CP energies determined experimentally (dots). The lines are the best fits to $E(x) = ax^2 + bx + c$ for the zigzag direction.

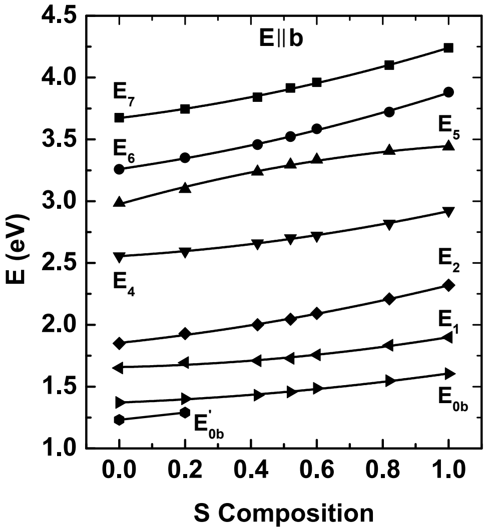

Figure 13. As Figure 12, but for the armchair direction.

Table 4. As Table 3, for the armchair direction.

CP	*c*	*b*	*a*
E'_{0b}	1.234	0.2939	0
E_{0b}	1.3716	0.1006	0.1341
E_1	1.6577	0.0555	0.1865
E_2	1.8535	0.2844	0.1815
E_4	2.5555	0.1627	0.2013
E_5	2.9756	0.7565	−0.2862
E_6	3.2598	0.3873	0.2298
E_7	3.6728	0.3259	0.2421

4. Conclusions

We report a systematic study of the composition dependence of the dielectric tensor along the zigzag and armchair directions, as measured on the cleavage plane of SnS_xSe_{1-x} alloys at room temperature using spectroscopic ellipsometry. The CP peak energies are determined from analysis of the numerical second derivative of the dielectric function for each principal direction. We found that the CP peaks have similar energy positions in the two perpendicular directions, even if their line-shapes are significantly different. The appearance of new CPs was observed in both armchair-and zigzag-directions when x is less than 0.2. Energy band structure calculations are performed using the mBJ method for bandgap correction, which enables the origins of the band-to-band transitions of the CPs to be determined. For example, the fundamental band gap of SnSe arises from an M_0 minimum, while that for SnS arises from an M_1 saddle point in SnS along the armchair axis. The composition dependence of the CPs is described by quadratic polynomial equations. The results extend our knowledge of the optical characteristics of SnS_xSe_{1-x} alloys, and should be helpful in the engineering of optoelectronic devices.

Author Contributions: X.A.N. conceived the major part of the SE experiments and analyzed. L.V.L. performed the band structure calculations. T.J.K. and Y.D.K. analyzed SE data and prepare the manuscript. T.M.H.N. and S.C. performed sample growing. T.H.N. and B.K. performed AFM measurement. K.K. and W.L. performed data filtering. All authors have read and agreed to the published version of the manuscript.

Funding: This research was supported by NATIONAL RESEARCH FOUNDATION OF KOREA (NRF) grant funded by the Korea government (MSIP) (NRF-2020R1A2C1009041) and The NATIONAL RESEARCH FOUNDATION OF KOREA (NRF) grant funded by the Korea government (NRF-2019R1H1A2079786).

Institutional Review Board Statement: Not applicable.

Informed Consent Statement: Not applicable.

Data Availability Statement: The study did not report any data.

Conflicts of Interest: The authors declare no conflict of interest.

References

1. Ai, J.; Zhao, X.; Lei, Y.; Yang, S.; Xu, Q.; Lai, C.; Peng, C. Pomegranate-inspired SnS/ZnS@C heterostructural nanocubes towards high-performance sodium ion battery. *Appl. Surf. Sci.* **2019**, *496*, 143631. [CrossRef]
2. Tang, H.; Li, Y.; Ye, H.; Hu, F.; Gao, C.; Tao, L.; Tu, T.; Gou, G.; Chen, X.; Fan, X.; et al. High-performance humidity sensor using Schottky-contacted SnS nanoflakes for noncontact healthcare monitoring. *Nanotechnology* **2020**, *31*, 055501. [CrossRef] [PubMed]
3. Jung, Y.W.; Yoon, J.J.; Kim, Y.D.; Woo, D. Study of the Interaction Between Biomolecule Monolayers Using Total Internal Reflection Ellipsometry. *J. Korean Phys. Soc.* **2020**, *58*, 1031–1034. [CrossRef]
4. Lefebvre, P.; Gil, B.; Allegre, J.; Mathieu, H.; Chen, Y. Nonparabolic behavior of GaSb-Alsb quantum wells under hydrostatic pressure. *Phys. Rev. B* **1987**, *35*, 1230–1235. [CrossRef] [PubMed]
5. Lukes, F.; Humlicek, J.; Schmidt, E. Electroreflectance and thermoreflectance spectra of SnS. *Solid State Commun.* **1983**, *45*, 445–448. [CrossRef]
6. Hegde, S.S.; Murahari, P.; Fernandes, B.J.; Venkatesh, R.; Ramesh, K. Synthesis, thermal stability and structural transition of cubic SnS nanoparticles. *J. Alloys Compd.* **2020**, *820*, 153116. [CrossRef]
7. Li, Z.; Sun, F.H.; Tang, H.; Dong, J.F.; Li, J.F. Enhanced thermoelectric properties of p-type SnS0.2Se0.8 solid solution doped with Ag. *J. Alloys Compd.* **2018**, *745*, 172–178. [CrossRef]
8. Zhao, D.; Wang, X.; Wu, D. Enhanced Thermoelectric Properties of Graphene/Cu2SnSe3 Composites. *Crystals* **2017**, *7*, 71. [CrossRef]
9. Shen, X.; Tang, C.; Zhang, C.; Li, G.; Zhao, Y.; Li, W.; Chen, G.; Yang, T. CuZnSn(SxSe1-x)4 Solar Cell Prepared by the Sol-Gel Method Following a Modified Three-Step Selenization Process. *Crystals* **2019**, *9*, 474. [CrossRef]
10. Butt, F.K.; Haq, B.; Rehman, S.U.; Ahmed, S.R.; Cao, C.; AlFaifi, S. Investigation of thermoelectric properties of novel cubic phase SnSe: A promising material for thermoelectric applications. *J. Alloys Compd.* **2017**, *715*, 438–444. [CrossRef]
11. Chu, F.; Zhang, Q.; Zhou, Z.; Hou, D.; Wang, L.; Jiang, W. Enhanced thermoelectric and mechanical properties of Na-doped polycrystalline SnSe thermoelectric materials via CNTs dispersion. *J. Alloys Compd.* **2018**, *741*, 756–764. [CrossRef]
12. Guan, X.; Lu, P.; Wu, L.; Han, L.; Liu, G.; Song, Y.; Wang, S. Thermoelectric properties of SnSe compound. *J. Alloys Compd.* **2015**, *643*, 116–120. [CrossRef]
13. Arepalli, V.K.; Kim, J. Effect of substrate temperature on the structural and optical properties of radio frequency sputtered tin sulfide thin films for solar cell application. *Thin Solid Films* **2018**, *666*, 34–39. [CrossRef]
14. Cho, J.Y.; Shin, K.; Lee, H.S.; Neerugatti, K.E.; Heo, J. Influence of sodium diffusion from substrates on performance of SnS/CdS thin-film solar cells. *J. Mater. Chem. A* **2019**, *7*, 24186–24190. [CrossRef]
15. Choi, H.; Lee, N.; Park, H.; Choi, Y.; Kim, K.; Choi, Y.; Kim, J.; Song, S.; Yuk, H.; Jeon, H. Development of a SnS film process for energy device applications. *Appl. Sci.* **2019**, *9*, 4606. [CrossRef]

16. Chua, D.; Kim, S.B.; Sinsermsuksakul, P.; Gordon, R. Atomic layer deposition of energy band tunable tin germanium oxide electron transport layer for the SnS-based solar cells with 400 mV open-circuit voltage. *Appl. Phys. Lett.* **2019**, *114*, 213901. [CrossRef]
17. Shown, I.; Samireddi, S.; Chang, Y.C.; Putikam, R.; Chang, P.H.; Sabbah, A.; Fu, F.Y.; Chen, W.F.; Wu, C.I.; Yu, T.Y.; et al. Carbon-doped SnS2 nanostructure as a high-efficiency solar fuel catalyst under visible light. *Nat. Commun.* **2018**, *9*, 169. [CrossRef]
18. Chao, D.; Zhu, C.; Yang, P.; Xia, X.; Liu, J.; Wang, J.; Fan, X.; Savilov, S.V.; Lin, J.; Fan, H.J.; et al. Array of nanosheets render ultrafast and high-capacity Na-ion storage by tunable pseudocapacitance. *Nat. Commun.* **2016**, *7*, 12122. [CrossRef]
19. Wang, S.F.; Wang, W.; Fong, W.K.; Yu, Y.; Surya, C. Tin Compensation for the SnS Based Optoelectronic Devices. *Sci. Rep.* **2017**, *7*, 39704. [CrossRef]
20. Bushell, Z.L.; Broderick, C.A.; Nattermann, L.; Joseph, R.; Keddie, J.L.; Rorison, J.M.; Volz, K.; Sweeney, S.J. Giant bowing of the band gap and spin-orbit splitting energy in GaP 1−xBix dilute bismide alloys. *Sci. Rep.* **2019**, *9*, 1–8. [CrossRef]
21. Bedair, T.M.; Cho, Y.; Kim, T.J.; Kim, Y.D.; Park, B.J.; Joung, Y.K.; Han, D.K. Reinforcement of interfacial adhesion of a coated polymer layer on a cobalt-chromium surface for drug-eluting stents. *Langmuir* **2014**, *30*, 8020–8028. [CrossRef] [PubMed]
22. Wei, W.; Wang, J.; Liu, Y.; Peng, Y.; Maraj, M.; Peng, B.; Wang, Y.; Sun, W. Effects of Thermal Annealing on Optical Properties of Be-Implanted GaN Thin Films by Spectroscopic Ellipsometry. *Crystals* **2020**, *10*, 439. [CrossRef]
23. Zalamai, V.V.; Rusu, E.V.; Syrbu, N.N.; Tiron, A.V. Optical properties and electronic band structure of SnS single crystals. *Phys. B Condens. Matter* **2019**, *575*, 411712. [CrossRef]
24. Rehman, S.U.; Butt, F.K.; Hayat, F.; Haq, B.; Tariq, Z.; Aleem, F.; Li, C. An insight into a novel cubic phase SnSe for prospective applications in optoelectronics and clean energy devices. *J. Alloys Compd.* **2018**, *733*, 22–32. [CrossRef]
25. Cao, M.; Wu, C.; Yao, K.; Jing, J.; Huang, J.; Cao, M.; Zhang, J.; Lai, J.; Ali, O.; Wang, L.; et al. Chemical bath deposition of single crystal SnS nanobelts on glass substrates. *Mater. Res. Bull.* **2018**, *104*, 244–249. [CrossRef]
26. Rana, C.; Saha, S. Structural, optical and electrical characterization of SnS nanomaterials grown at different temperatures. *J. Mater. Sci. Mater. Electron.* **2019**, *30*, 21160–21169. [CrossRef]
27. Mirabella, F.; Ghijsen, J.; Johnson, R.L.; Golacki, Z.; Orlowski, B.A. Photoemission study of Sn1-xMnxSe2. *J. Alloys Compd.* **2001**, *328*, 166–170. [CrossRef]
28. Raadik, T.; Grossberg, M.; Raudoja, J.; Traksmaa, R.; Krustok, J. Temperature-dependent photoreflectance of SnS crystals. *J. Phys. Chem. Solids* **2019**, *74*, 1683–1685. [CrossRef]
29. Losurdo, M.; Bergmair, M.; Bruno, G.; Cattelan, D.; Cobet, C.; De Martino, A.; Fleischer, K.; Dohcevic-Mitrovic, Z.; Esser, N.; Galliet, M.; et al. Spectroscopic ellipsometry and polarimetry for materials and systems analysis at the nanometer scale: State-of-the-art, potential, and perspectives. *J. Nanopart. Res.* **2009**, *11*, 1521–1554. [CrossRef]
30. Aspnes, D.E.; Studna, A.A. Dielectric functions and optical parameters of Si, Ge, GaP, GaAs, GaSb, InP, InAs, and InSb from 1.5 to 6.0 eV. *Phys. Rev. B* **1983**, *27*, 985. [CrossRef]
31. Logothetidis, S.; Via, L.; Cardona, M. Temperature dependence of the dielectric function and the interband critical points of InSb. *Phys. Rev. B* **1985**, *31*, 947–957. [CrossRef] [PubMed]
32. Logothetidis, S.; Polatoglou, H.M. Ellipsometric studies of the dielectric function of SnSe and a simple model of the electronic structure and the bonds of the orthorhombic IV-VI compounds. *Phys. Rev. B* **1987**, *36*, 7491. [CrossRef] [PubMed]
33. Banai, R.E.; Burton, L.A.; Choi, S.G.; Hofherr, F.; Sorgenfrei, T.; Walsh, A.; To, B.; Cröll, A.; Brownson, J.R.S. Ellipsometric characterization and density-functional theory analysis of anisotropic optical properties of single-crystal α-SnS. *J. Appl. Phys.* **2014**, *116*, 013511. [CrossRef]
34. Nguyen, H.T.; Le, V.L.; Nguyen, T.M.H.; Kim, T.J.; Nguyen, X.A.; Kim, B.; Kim, K.; Lee, W.; Cho, S.; Kim, Y.D. Temperature Dependence of the Dielectric Function and Critical Points of α-SnS from 26 to 350 K. *Sci. Rep.* **2020**, *10*, 18396. [CrossRef] [PubMed]
35. Le, V.L.; Cuong, D.D.; Nguyen, X.A.; Nguyen, H.T.; Nguyen, T.M.H.; Cho, S.; Hong, S.C.; Rhim, S.H.; Kim, T.J.; Kim, Y.D. Anisotropic Behavior of Excitons in Single Crystal α-SnS. *AIP Adv.* **2020**, *10*, 105003. [CrossRef]
36. Ly, T.T.; Duvjir, G.; Min, T.; Byun, J.; Kim, T.; Saad, M.M.; Hai, N.T.M.; Cho, S.; Lee, J.; Kim, J. Atomistic study of the alloying behavior of crystalline SnSe1-xSx. *Phys. Chem. Chem. Phys.* **2017**, *19*, 21648–21654. [CrossRef]
37. Nguyen, T.M.H.; Nguyen, Q.V.; Duong, A.T.; Cho, S. Growth and electrical properties of $SnS_{1\text{-}x}Se_x$ ($0 \le x \le 1$) single crystals grown using the temperature gradient method. *J. Korean Phys. Soc.* **2021**. [CrossRef]
38. Aspnes, D.E. Approximate solution of ellipsometric equations for optically biaxial crystals. *J. Opt. Soc. Am.* **1980**, *10*, 1275–1277. [CrossRef]
39. Logothetidis, S.; Via, L.; Cardona, M. Ellipsometric study of interband transitions in orthorhombic GeS. *Phys. Rev. B* **1985**, *31*, 2180. [CrossRef]
40. Schubert, M.; Hofmann, T.; Herzinger, C.M.; Dollase, W. Generalized ellipsometry for orthorhombic, absorbing materials: Dielectric functions, phonon modes and band-to-band transitions of Sb2S3. *Thin Solid Film.* **2004**, *455–456*, 619–623. [CrossRef]
41. Jellison, G.E., Jr.; McGuire, M.A.; Boatner, L.A.; Budai, J.D.; Specht, E.D.; Singh, D.J. Spectroscopic dielectric tensor of monoclinic crystals: CdWO4. *Phys. Rev. B* **2011**, *84*, 195439. [CrossRef]
42. Schmidt, D.; Booso, B.; Hofmann, T.; Schubert, E.; Sarangan, A.; Schubert, M. Generalized ellipsometry for monoclinic absorbing materials: Determination of optical constants of Cr columnar thin films. *Opt. Lett.* **2009**, *34*, 992. [CrossRef] [PubMed]

43. Wong, T.K.S.; Gong, Y.; Yang, P.; Ng, C.M. Characterization of biaxial stressed silicon by spectroscopic ellipsometry and synchrotron x-ray scattering. *Semicond. Sci. Technol.* **2007**, *22*, 1232. [CrossRef]
44. Bruggeman, D.A.G. Berechnung verschiedener physikalischer Konstanten von heterogenen substanzen. *Ann. Phys.* **1953**, *416*, 636. [CrossRef]
45. Blöchl, P.E. Projector augmented-wave method. *Phys. Rev. B* **1994**, *50*, 17953–17979. [CrossRef]
46. Perdew, J.P.; Chevary, J.A.; Vosko, S.H.; Jackson, K.A.; Pederson, M.R.; Singh, D.J.; Fiolhais, C. Erratum: Atoms, molecules, solids, and surfaces: Applications of the generalized gradient approximation for exchange and correlation. *Phys. Rev. B* **1993**, *48*, 4978. [CrossRef]
47. Perdew, J.P.; Burke, K.; Ernzerhof, M. Generalized gradient approximation made simple. *Phys. Rev. Lett.* **1996**, *77*, 3865–3868. [CrossRef]
48. Becke, A.D.; Johnson, E.R. A simple effective potential for exchange. *J. Chem. Phys.* **2006**, *124*, 221101. [CrossRef]
49. Tran, F.; Blaha, P. Accurate band gaps of semiconductors and insulators with a semilocal exchange-correlation potential. *Phys. Rev. Lett.* **2009**, *102*, 5–8. [CrossRef]
50. Chandrasekhar, H.R.; Humphreys, R.G.; Zwick, U.; Cardona, M. Infrared and Raman spectra of the IV–VI compounds SnS and SnSe. *Phys. Rev. B* **1977**, *15*, 2177–2183. [CrossRef]
51. Luo, W.; Ismail-Beigi, S.; Cohen, M.L.; Louie, S.G. Quasiparticle band structure of ZnS and ZnSe. *Phys. Rev. B* **2002**, *66*, 195215. [CrossRef]
52. Waler, J.P.; Cqhen, M.L. Calculation of the Refiectivity, Modulated Refiectivity, and Band Structure of GaAs, GaP, ZnSe, and ZnS. *Phys. Rev.* **1969**, *183*, 763. [CrossRef]
53. Erbarut, E. Optical response functions of ZnS, ZnSe, ZnTe by the LOM method. *Solid State Commun.* **2003**, *127*, 515–519. [CrossRef]
54. Gomes, L.C.; Trevisanutto, P.E.; Carvalho, A.; Rodin, A.S.; Neto, A.H.C. Strongly bound Mott-Wannier excitons in GeS and GeSe monolayers. *Phys. Rev. B* **2016**, *94*, 1–5. [CrossRef]
55. Eymard, R.; Otto, A. Optical anil electron-energy-loss spectroscopy of GeS, GeSe, SnS, anil SnSe single crystals. *Phys. Rev. B* **1977**, *16*, 541–559. [CrossRef]
56. Cardona, M. *Modulation Spectroscopy*, 1st ed.; Academic Press: Cambridge, MA, USA, 1969; Volume 11.
57. Le, V.L.; Kim, T.J.; Kim, Y.D.; Aspnes, D.E. Combined interpolation, scale change, and noise reduction in spectral analysis. *J. Vac. Sci. Technol. B* **2019**, *37*, 052903. [CrossRef]
58. Le, V.L.; Kim, T.J.; Kim, Y.D.; Aspnes, D.E. External removal of endpoint-discontinuity artifacts in the reciprocal-space analysis of spectra. *Curr. Appl. Phys.* **2020**, *20*, 232–236. [CrossRef]
59. Lautenschlager, P.; Garriga, M.; Vina, L.; Cardona, M. Temperature dependence of the dielectric function and interband critical points in silicon. *Phys. Rev. B* **1987**, *36*, 4821. [CrossRef] [PubMed]
60. Lautenschlager, P.; Garriga, M.; Cardona, M. Temperature dependence of the interband critical-point parameters of InP. *Phys. Rev. B* **1987**, *36*, 4813. [CrossRef]
61. Zollner, S.; Garriga, M.; Kircher, J.; Humlicek, J.; Cardona, M.; Neuhold, G. Temperature dependence of the dielectric function and the interband critical-point parameters of GaP. *Phys. Rev. B* **1993**, *48*, 7915. [CrossRef] [PubMed]
62. Kim, J.Y.; Yoon, J.J.; Kim, T.J.; Kim, Y.D.; Lee, E.H.; Bae, M.H.; Song, J.D.; Choi, W.J.; Liang, C.T.; Chang, Y.C. Optical properties of AlAsxSb1-x alloys determined by in situ ellipsometry. *Appl. Phys. Lett.* **2013**, *103*, 011901. [CrossRef]
63. Davydov, Y.V.; Goncharuk, I.N.; Smirnov, A.N.; Nikolaev, A.E.; Lundin, W.V.; Usikov, A.S.; Klochikhin, A.A.; Aderhold, J.; Graul, J.; Semchinova, O.; et al. Composition dependence of optical phonon energies and Raman line broadening in hexagonal (formula presented) alloys. *Phys. Rev. B* **2002**, *65*, 125203. [CrossRef]
64. Lu, X.; Beaton, D.A.; Lewis, R.B.; Tiedje, T.; Zhang, Y. Composition dependence of photoluminescence of GaAs1-xBix alloys. *Appl. Phys. Lett.* **2009**, *95*, 129–132. [CrossRef]